

Fracture Assessment of Carbon Fibre/Epoxy Reinforcing Rings through a Combination of Full-Scale Testing, Small-Scale Testing and Stress Modeling

Pieter Samyn • Ludo Van Schepdael •
Wim Van Paepegem • J.S. Leendertz • Eric Suister •
Patrick De Baets • Joris Degrieck

Received: 18 November 2005 / Accepted: 28 February 2006
© Springer Science + Business Media, Inc. 2006

Abstract Carbon fibre/epoxy rings are used as radial reinforcement for polymer bearing elements with nominal diameter 250 mm functioning under 150 MPa. Full-scale static and dynamic testing revealed no catastrophic failure for loading to 400 MPa, although there was circumferential splitting of carbon fibres at the machined top edge causing counterface wear under sliding. A combined numerical–experimental analysis was applied for design improvement with a representative small-scale qualification test on the real ring geometry, inducing additional stress concentrations compared to ASTM standards. Full-scale modelling revealed high *radial–axial* shear stresses (33 MPa) in non-hydrostatically loaded zones, while it increased towards 104 MPa under hydrostatic load conditions. The former is the most critical and should be simulated either on a small-scale unidirectional compression test or on a representative short beam shear test, respectively, measuring the *radial–axial* or *radial–tangential* shear strength. A relation between both small-scale states of stress was experimentally and numerically studied, experiencing that the composite ring has lower radial–tangential shear stress compared to radial–axial shear stress as a different hydrostatic stress state is observed in the bulk of the composite ring. As a compressive test is however more difficult to perform than a short-beam-shear test, a representative design criterion for shear fracture is determined from failure at 27 kN normal load in a short-beam-shear test. Finally,

P. Samyn (✉) • W. Van Paepegem • P. De Baets • J. Degrieck
Laboratory Soete, Department Mechanical Construction and Production,
Ghent University, St. Pietersnieuwstraat 41, B-9000 Gent, Belgium
e-mail: pieter.samyn@UGent.be

L. Van Schepdael
SOLICO B.V., Solutions in Composites, Everdenberg 97,
NL-4902 TT Oosterhout, The Netherlands

J.S. Leendertz • E. Suister
Ministry of Transport, Public Works and Water Management, Directorate-General,
Herman Gorterhove 4, NL-2700 AB Zoetermeer, The Netherlands

fracture is avoided by optimising the cross-sectional geometry of the composite reinforcing ring and close control of the processing parameters.

Key words finite elements · full-scale · shear failure · small-scale

1. Introduction

Carbon-fibre-reinforced epoxy (CFR-E) composites are finding increasing use in structural applications due to their high strength and lightweight properties. Recently, filament wound CFR-E rings are introduced as radial reinforcement for ultra-high-molecular-weight polyethylene (UHMWPE) pads that are placed as sliding components in the Maeslant storm surge barrier near Rotterdam (NL) [1]. Although a polymer component has favourable friction and wear characteristics, its loading capacity is limited and the qualities of the CFR-E reinforcement determine whether the structure withstands the combination of extremely high normal loads and frictional shear stresses. A similar reinforcing methodology seems favourable for reparation of damaged concrete cylinders [2]. As delamination and shear are the most critical failure mechanisms for composite materials [3], they should be avoided by good design and close control of material production parameters. Delamination or interlaminar fracture may lead to loss in stiffness and extrusion of UHMWPE, with loss of functionality and bearing capacity because of changes in clearance between the convex and concave sliding surfaces.

The resistance against delamination is characterised by the interlaminar shear strength (ILSS), defined as the shear stress at rupture where the plane of fracture is located between two layers of reinforcement of the carbon ring. The initiation and growth of a delamination crack is mainly dictated by interlaminar normal stresses. In addition, process-induced defects grow easily parallel to the fibre direction, resulting in interlaminar ‘hear’ fracture. One important factor is the fibre-matrix interface, also influenced by the matrix texture: a small-size mosaic structure suggests a strong fibre-matrix bonding and consequently high ILSS. At the same time, brittle fracture was however observed while a matrix with large domains lead to pseudo-plastic failure [4]. Several testing methods are available for measuring the strength of anisotropic materials. The main characterisation for ILSS is the short-beam-shear test (ASTM D-2344-00), the four-point shear test, the Iosipescu test (ASTM D-5379-98), the tensile test (ASTM D-3518-94) and the double notch compression test (ASTM D-3846-94). However, it was demonstrated by Li et al. [5] how the ILSS depends on the test method: for example in the short-beam test a non-uniform bending moment along the shear plane and stress concentrations under the loading rollers may yield undesirable errors while the distribution of the shear stresses over the shear planes (laminar planes) introduces a difficulty to analysis [6]; a compression test leads to lower shear strength as the failure consistently occurs in a well-defined single shear plane [7], yielding a rather conservative estimate for safety design. Consequently, it can be guessed that also the relation between small-scale test methods and a real on-the-field fracture test yields different results due to variations in stress conditions and test geometries.

A combined numerical–experimental approach of fracture phenomena on reinforced polymer bearing elements observed after full-scale static and dynamic testing is presented in this paper. Experimental results on static loading [8] and

tribological behaviour [9] were used as qualification test data, presently analysed by finite element modelling for quantification of the internal stresses. Although full-scale tests are the most reliable, they are time-consuming and should be translated into representative small-scale tests. One problem is that the fracture mode is influenced by the boundary conditions and sample geometry, and standardised sample geometries often cannot be applied. Therefore, appropriate testing conditions determined from full-scale tests are used as input for small-scale tests and a fracture criterion based on representative small-scale tests is designed, taking into account the specific stress conditions. An international test program in parallel to an optimisation of the design process of the composite CFR-E ring was therefore performed at Ghent University (Laboratory Soete) and Solico (Solutions in Composites) while the final bearing concept was implemented and proven on-the-field by the Nederlandse Rijkswaterstaat.

2. Experimental

2.1. Test Geometry

A composite bearing element as shown in Figure 1 has a nominal diameter of 249.5 mm and a thickness of 40 mm. For functioning as sliding pad, it will be incorporated in a steel hole with nominal diameter 250 mm and depth 32 mm. As such, the UHMWPE sliding surface is 8 mm above the steel surface and should be dimensionally stabilised by a carbon fibre/epoxy ring. Contact between the sliding counterface and the reinforcing CFR-E ring should however be avoided due to unfavourable friction and wear characteristics. Therefore, a polymer lip with diameter 237 mm was experimentally designed and protects the CFR-E ring through cold flow between the top surface of the ring and the counterface.

The central UHMWPE part consists of compression moulded GUR 4120 [10] with intrinsic viscosity 2,400 ml/g, density 0.93 g/cm³, average molecular weight of 5.10⁶ g/mol. The material is isotropic with elasticity modulus $E = 720$ MPa and Poisson coefficient $\nu = 0.45$. The compressive yield strength is 21 MPa.

The reinforcing composite ring has a nominal outer diameter of 249.0 mm and is made of unidirectional carbon fiber Toray T700 12K (1.8 g/cm³) and epoxy Bakelite

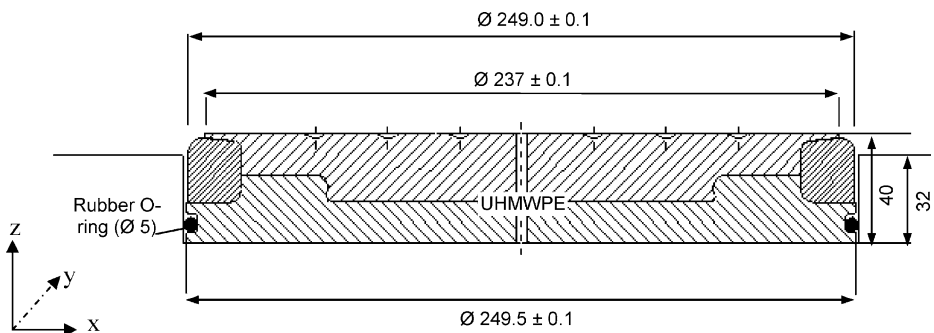


Figure 1 Full-scale composite bearing element (diameter 249.5 mm) with radial reinforcing carbon fibre/epoxy ring of diameter 249.0 mm in machined hole of diameter 250.0 mm (sample holder)

EPR-LB20 HXS resin with EPH 960 hardener (1.090 g/cm^3), further indicated as 'Resin A.' A second industrial epoxy resin is used (1.175 g/cm^3), further indicated as 'Resin B.' The nominal radial thickness is 20 and 24 mm axial height. A filament winding process over a 104.5 mm steel mandrel with winding angle 90° is applied (the rings are afterwards machined), as Liu et al. [11] compared 45° , 60° and 90° winding for E-glass fibre/epoxy radial reinforcements on concrete cylinders, concluding that a 90° reinforcement has highest axial compressive strength and a 45° lowest strength. Combinations with layer sequences along various winding angles have intermediate strength. The material is transversally isotropic as it is only fibre-reinforced in the hoop winding direction, with elasticity constants $E_y = 150 \text{ GPa}$ (fibre direction) and $E_x = E_z = 9 \text{ GPa}$ (radial and axial directions); Poisson coefficients $\nu_{xy} = \nu_{yz} = 0.34$ and $\nu_{xz} = 0.5$; shear moduli $G_{xy} = G_{yz} = 4 \text{ GPa}$ and $G_{xz} = 3 \text{ GPa}$ (orientations according to Figure 1). It should have fibre percentages between 58%–63% and a porosity content $<2.5\%$. Its thermal properties are determined from a DSC-test with $T_G > 95^\circ \text{C}$ and from a DMTA-test with $T_G > 105^\circ \text{C}$. The curing times and temperatures were strictly controlled at 16 hrs room temperature, 8 to 10 h at 60°C and 8 to 10 h at 120°C with 15°C per hour temperature raise. The resulting tensile stress in fibre direction $\sigma_x = 2450 \text{ MPa}$. The shear strength however strongly depends on the composition and production parameters: The determination of a reliable value is subject of present investigation. It is important for the dimensional stability of the hybrid UHMWPE discs that the carbon fibre/epoxy rings are fitted on the UHMWPE pad at room temperature.

2.2. Test Program

As calculated from final element analysis of the construction, the contact pressure on one single bearing element attains either 163 or 147 MPa (averaged 150 MPa) under working conditions. *Full-scale* static loading tests on bearing elements with diameter 249.50 mm are done on a hydraulic vertical press with maximum capacity of 10,000 kN (Figure 2(a)). Specimens are incorporated in a sample holder with diameter 250.00 mm and depth 32 mm according to the boundary conditions in the practical bearing application. It is the aim to determine the stiffness under compressive loading, maximum vertical indentation and failure on the retaining action of the carbon fibre/epoxy reinforcing ring, when loaded by a convex counterface with radius 5,000 mm. Details about the test set-up and test results are discussed in another report [8]. Full-scale sliding tests are done on a large-scale tribometer (Figure 2(b)) under 15 to 150 MPa contact pressure and 0.005 m/s sliding velocity with a flat Zn-coated steel counterface, determining wear and friction coefficients with the effect of horizontal shear stresses on failure of the CFR-E reinforcement. The dynamic test conditions and experimental results are detailed elsewhere [9]. Full-scale tests are presently used as they induce multiaxial loading of the composite structure with a *hydrostatic stress condition* and take into account the internal stresses after fabrication.

For *small-scale* verification on the shear strength of the CFR-E reinforcing ring, short-beam shear tests (*SBS*) and unidirectional compression tests (*UC*) on a separate ring are used. It will be verified whether a small-scale test is representative for previous full-scale tests. Both small-scale test set-ups are shown in Figure 3(a) and (b). However, the specific geometry and composition of the carbon fibre/epoxy

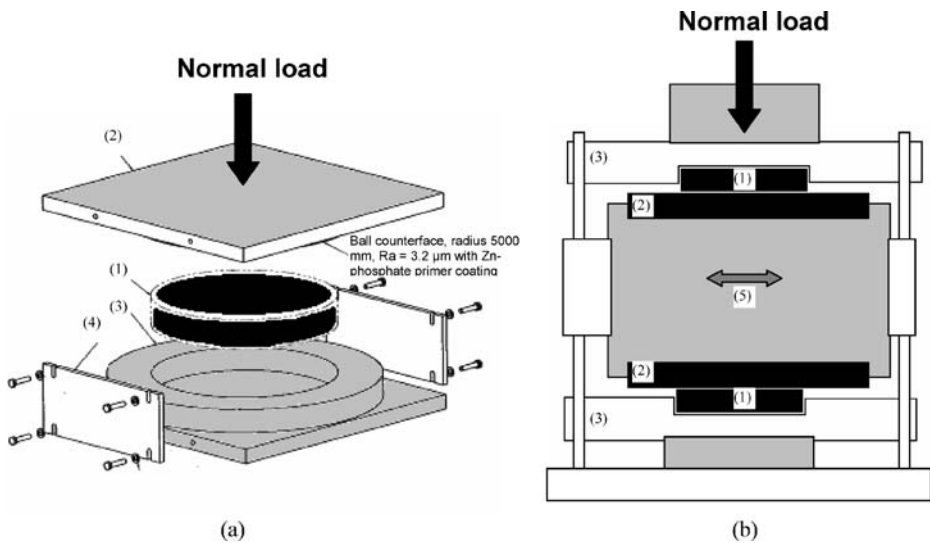


Figure 2 Experimental full-scale test equipment for (a) static compressive testing, (b) dynamic sliding testing with (1) CFR-E ring reinforced bearing element (\varnothing 249.5 mm), (2) counterface, (3) sample holder (\varnothing 250.0 mm), (4) clamps, (5) reciprocating sliding bloc

rings did not allow for testing standardised sample geometries, but an indication of the sample geometry is also given in mentioned figures:

- The *SBS-test* is used for determination of the *radial-tangential* shear strength or ILSS (parallel to fibre orientation), based on ASTM D2344-84: “Apparent interlaminar shear strength of parallel fibre composites by short-beam method” or ISO 14130-1997: “Fibre-reinforced plastic composites – Determination of interlaminar shear strength by short beam method.” The ASTM standard for testing carbon fibre composites requires a span-to-thickness ratio of 4.0 and a length-to-thickness ratio of 6.0. For present design test (called ‘*the Maeslant test*’) however, the original radial ring thickness of 20 mm with machined edge will be maintained with a span of 80 mm (ratio 4.0) since reducing the ring thickness would imply additional machining and the ILSS depends on span-to-thickness ratio [12]. A specimen with outer curvature radius 124.5 mm and inner curvature radius 104.5 mm was placed on two flat supports that allow lateral motion while a load was applied at the centre of the ring segment. For present large sample thickness and span, the use of circular supports was not favourable and flat supports with radii 2 mm were applied. A pin with radius 5 mm is used. An investigation of different load nose diameters was performed by Cui et al. [13] who determined that larger diameters reduced the contact stress concentration and avoided compressive failure under the roller. The fact that it is a simple test makes the SBS method attractive as a material screening or quality control test as presently used. To validate test results, they will be compared to the standardised ring thickness of 6 mm with a span of 24 mm. The tests were performed on an Instron 4,505 testing frame at room temperature using a 100 kN load cell with a cross-head speed of 1.3 mm/min. The failure load was

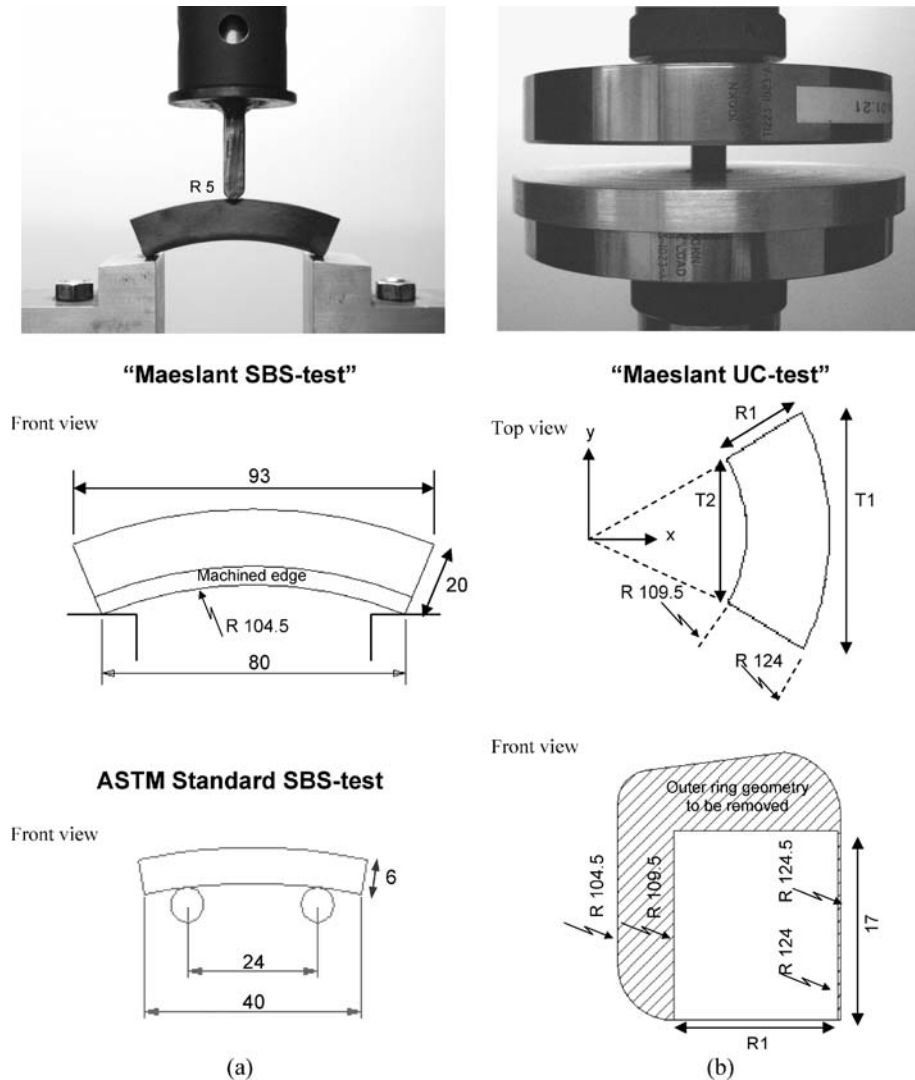


Figure 3 Experimental small-scale test equipment and sample geometry for fit-to-purpose Maeslant tests (a) short beam shear test (*front view*), (b) uniaxial compression test (*top and front view*)

interpreted as the first maximum load attained. The apparent shear strength was calculated using the formula 1 (ASTM D2344-00):

$$\tau_{\max} = \frac{3}{4} \frac{F_N}{wt} \quad (1)$$

where F_N is the normal load at failure, w is the width and t is the thickness of the specimen. The nominal cross-section area is 453 mm². Formula (1) is derived from elementary beam theory which assumes shear stresses to vary parabolic

through the thickness. Therefore, formula (1) represents the mean apparent shear strength, while finite element analysis will be used for illustration of the shear stress distribution over the beam section and length. The shear stress distribution is skewed towards the surface of the specimen close to the loading or supporting points.

- The *UC-test* is used for determination of the *radial-axial* shear strength (perpendicular to fibre orientation), according to ASTM D695-77: “Standard test method for compressive properties of rigid plastics.” As the original CFR-E ring section is difficult for interpretation, pieces were machined from the bulk of the CFR-E ring with square cross-section and curved length. As this is a time-consuming operation with extremely high cost, only a limited number of UC-tests were performed. While placed between two circular compression plates, specimens are loaded on a Instron 4505 machine at room temperature with a calibrated load cell of 100 kN at 0.9 mm/min. In order to ensure good alignment between the centre line of the loading frame and the centre point of the specimen geometry, an additional positioning plate is placed on the lower compression plate containing a circular hole with diameter 20.5 mm for mounting the ring segment. From the average diagonals and *X-Y* coordinates in Figure 3, the centre of gravity is at (116.8291, 0) while the centre point of the circumferential circle is at (116.9627, 0). With a clearance of 0.3 mm for positioning the ring segment in on the circular plate, the total positioning error <0.5 mm. It was verified by elastic compression of an aluminium bloc in the extremities of the compression plate that the eccentricity is acceptable and not influences the test result. The compressive strength was calculated from formula 2:

$$\sigma_{\max} = \frac{F_N}{A_{\text{eff}}} \quad (2)$$

where F_N is the normal load at failure, A_{eff} is the effective surface calculated from measured values T_1 (16.4 mm < T_1 < 18.2 mm), T_2 (15.2 mm < T_2 < 16.5 mm) and $R_1 = 19.7$ mm. Small variations in geometry are attributed to the difficult machining operations. The sample thickness is 17 mm. The nominal contact surface area is 204.36 mm².

2.3. Finite Element Analysis Model

While using EMRC-NISA FEM software, three finite element models were applied for a simulation of the local deformation and stresses in a CFR-E reinforcing ring on *full-scale* loading, small-scale *SBS-test* and small-scale *UC-test*, with a mesh illustrated in Figure 4. The goal of finite element modelling is to assess stress concentrations implied by the characteristic sample geometry and to validate the state of stress in small-scale tests in accordance to full-scale tests.

- The *full-scale* model (Figure 4(a)) simulates the carbon ring as load transferring element between the central UHMWPE part and the steel holes. Therefore, a normal load in the centre of the bearing element is applied parallel to the *Z*-axis (axial direction) through a convex with radius 5,000 mm and a friction force is

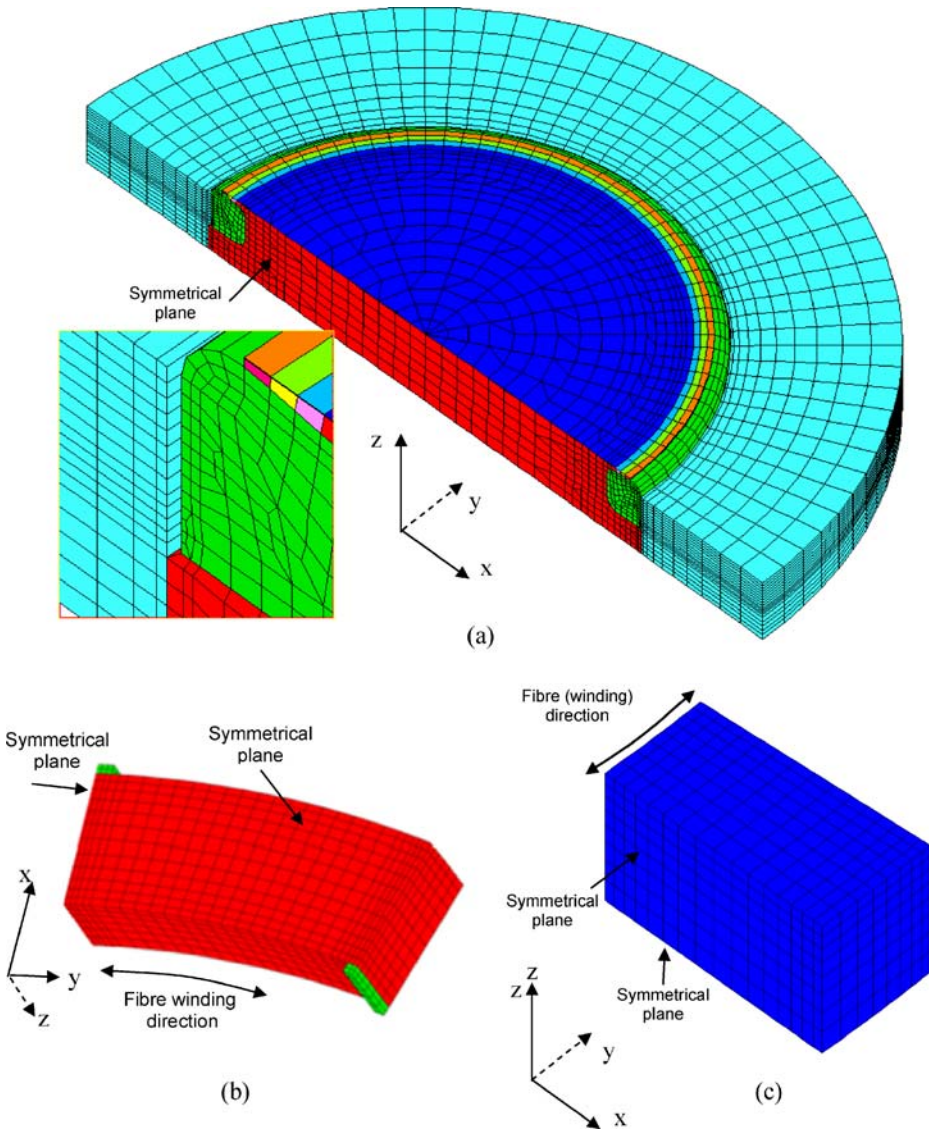


Figure 4 Finite element models for stress calculations on (a) full-scale test, and small-scale (b) SBS-test, (c) UC-test (Solico BV)

applied in X or radial direction (3D non-linear modelling). Nodes on the bottom are vertically fixed and horizontally free, assuming that no forces are transmitted through the bottom of the holder. On the radial edges, variable contact elements are used simulating the contact between the CFR-E ring and the steel holder. The initial clearance between the diameter of the bearing element and the steel holder is fixed at 0.75 mm. The steel part is modelled as a pure elastic material. Also the UHMWPE on top of the CFR-E ring (i.e., polymer lip) is modelled as pure elastic material (no visco-elastic properties or plastic deformation) in order

to avoid extrusion of polyethylene between the CFR-E ring and the convex counterface. The build-up of internal pressure under hydrostatic loading as experienced under real plastic conditions [8] is simulated by a gradual decrease of the polyethylene bulk modulus in the extrusion gap as shown on the detail insert of Figure 4(a). The symmetrical plane is simulated with zero normal displacement.

- The *SBS-tests* (Figure 4(b)) are linearly modelled with two symmetrical planes for a standard beam (square section), i.e., at the central loading point and at half-thickness, and a smaller mesh at the supporting points. For a beam with machined edges, the entire section is modelled. A normal load is applied along the *X*-axis (radial direction) with a pin radius 5 mm, the *Y*-axis is parallel to the fibre (tangential) direction and the *Z*-axis (axial direction) represents the sample thickness. Present orientation corresponds to full-scale tests. Different cuts are studied along the radial direction and at different thickness perpendicular to the loading pin. A comparison between linear and non-linear finite element analysis on SBS specimens [14] demonstrated that the difference in stress is small (<4%).
- The *UC-tests* (Figure 4(c)) are modelled on one quarter of the CFR-E specimen, due to symmetry conditions, with the normal load applied on the top surface parallel to the *Z*-axis (axial). The fibre (tangential) direction is parallel to the *Y*-axis and the *X*-axis is the radial direction. Present orientation corresponds to full-scale tests. The surface in contact with the compression plate is flat, although different friction conditions at the contact surface will be carefully considered. Linear calculations are performed on the CFR-E ring segment.

3. Full-Scale Test Results

3.1. Static and Dynamic Test Results

Experimental results on vertical indentation of a bearing element during static loading at 30, 60, 90, 120 and 150 MPa are given in Table I, together with static and dynamic coefficients of friction (μ_{stat} , μ_{dyn}) under sliding on the UHWMPE surface. A maximum design value is calculated from the latter values, occurring either under static friction, dynamic friction or after creep, wear and ageing. On-line registration

Table I Experimental full-scale test results for reinforced UHWMPE bearing elements under static (vertical indentation) and dynamic (friction) testing.

Contact Pressure (MPa)	Vertical Indentation			Coefficient of Friction		
	Immediate		After 2 h Creep (mm)	μ_{stat}	μ_{dyn}	$\mu_{\text{max, design}}$
	(mm)	(%)				
30	1.76	4.40	1.79	0.10	0.07	0.21
60	2.46	6.15	2.50	0.05	0.04	0.15
90	2.97	7.43	3.02	0.04	0.03(5)	0.09
120	3.42	8.55	3.48	0.03(5)	0.03	0.07
150	3.78	9.45	3.89	0.03	0.02(5)	0.06

of the vertical compression and the influences of creep and clearance between the bearing element and the sample holder were studied [8]: through the retaining action of the steel sample holder, there is a gradual increase in stiffness (bulk modulus) from 720 towards 4,910 MPa until a maximum load carrying capacity of 400 MPa is noticed, satisfying for emerging running-conditions. The permanent radial deformation of the carbon ring is between 0.07 and 0.17 mm, showing that it bears the deformation at 150 MPa. Eventual fracture of the carbon fibre/epoxy ring as described below did not result in an unstable stress-strain characteristic with sudden drop in normal load or increase in vertical indentation as it was observed by Kugler et al. [15], showing that present failure was not catastrophic.

3.2. Full-Scale Fracture Phenomena

Visual inspection of the CFR-E reinforcing ring is only done after a final load of 150 MPa. As shown on side-view photographs of the bearing element in Figure 5, the CFR-E ring failed at the top edge either after dynamic or static tests. Circumferential splitting of carbon fibres was observed in the zone above the machined shoulder edge. This ring-type splitting along the hoop winding direction was identically observed by Liu et al. [2, 11] for E-glass fibre/epoxy composites and characteristic for 90° winding angles. Failure was attributed to inter- or intralaminar delamination and could be reduced by non-adhesive filament winding or the use of hybrid composites. An aluminium foil was practically inserted foil between the original structure and reinforcing composite, preventing shear stress transfer. Nevertheless, delamination associated with the bending stress under expansion still occurred. Presently, the reinforcement design will be studied more in detail with stress modelling and modification of the original reinforcement section. Consequently, the fracture behaviour of different CFR-E ring cross-sections was experimentally tested as shown in Figure 6, with, respectively, straight edges, inclined edges with variable angle and round edges. The machined ring geometries were applied for avoiding direct contact between the CFR-E ring and the Zn-phosphate coated steel counterface, as it implied unacceptable high friction and counterface wear. Contact between the CFR-E ring and the convex counterface is finally avoided by design of a polymer lip with appropriate thickness and diameter [16]. In each case however, an identical fracture pattern of the CFR-E ring is observed with internal cracks initiating either at the onset of the machined edge, either in the centre of the machined edge or on top of the carbon ring in contact with the polymer lip. Although a specific curvature radius $R = 1$ to 4 mm is required, fine cracks are observed at the onset of the machined edge over the entire ring. Crack propagation in the bulk of the composite ring is observed under 30° to 45°, possibly dividing into multiple cracks. Fracture either proceeds towards the top surface of the ring or stabilises in the composite bulk. The direction of propagation is ensured by progressive narrowing of the crack from a wide initiation point. As no transverse cracks were observed, the structural integrity and strength of the CFR-E ring under full load is not affected and ensures the retaining of the central polyethylene part. However, when cracks propagate through the entire composite bulk under certain slope, edges are lost and separate carbon fibres detach from the bulk. Once free and mixed in the contact surface they cause catastrophic counterface wear and notably higher friction (0.07) compared to clean UHMWPE friction

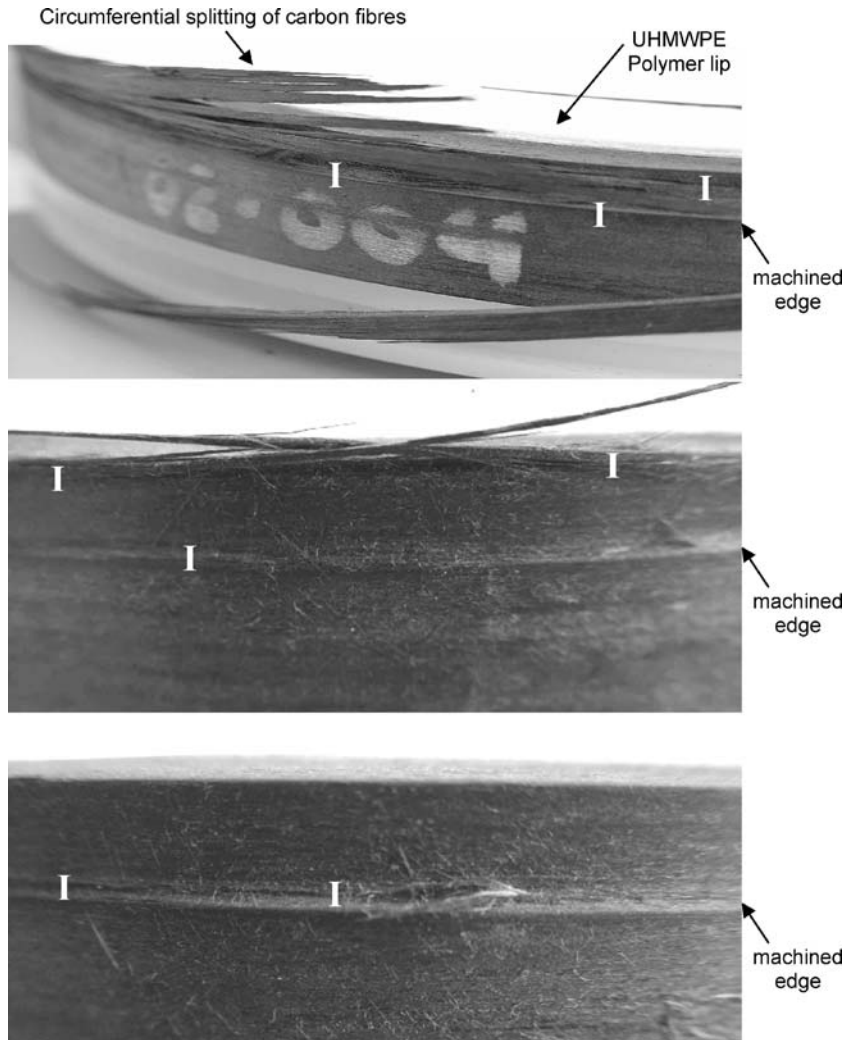


Figure 5 Macroscopic fracture of CFR-E reinforcing rings after full-scale loading at 150 MPa (*side views of bearing elements with indication of initiation points I*)

(0.02(5)) under 150 MPa working conditions. Failure of the ring edges also cause unstable polymer lip deformation.

The tendency for cracking is reduced for the final design with round edges, although fine crack initiation is still observed without propagation towards the top surface of the ring and less detrimental wear. In 50% of the tests on round edged CFR-E reinforcing rings no cracks were observed, even not after polishing. For reliable application, this uncertainty is not allowable and needs further understanding on the nature and influencing factors for failure. Based on the typical observed crack direction, internal delamination of the CFR-E composite under concentrated shear forces is most assumable and is further analysed by finite element models. Nevertheless, the cracks not completely disappear after reducing stress concen-

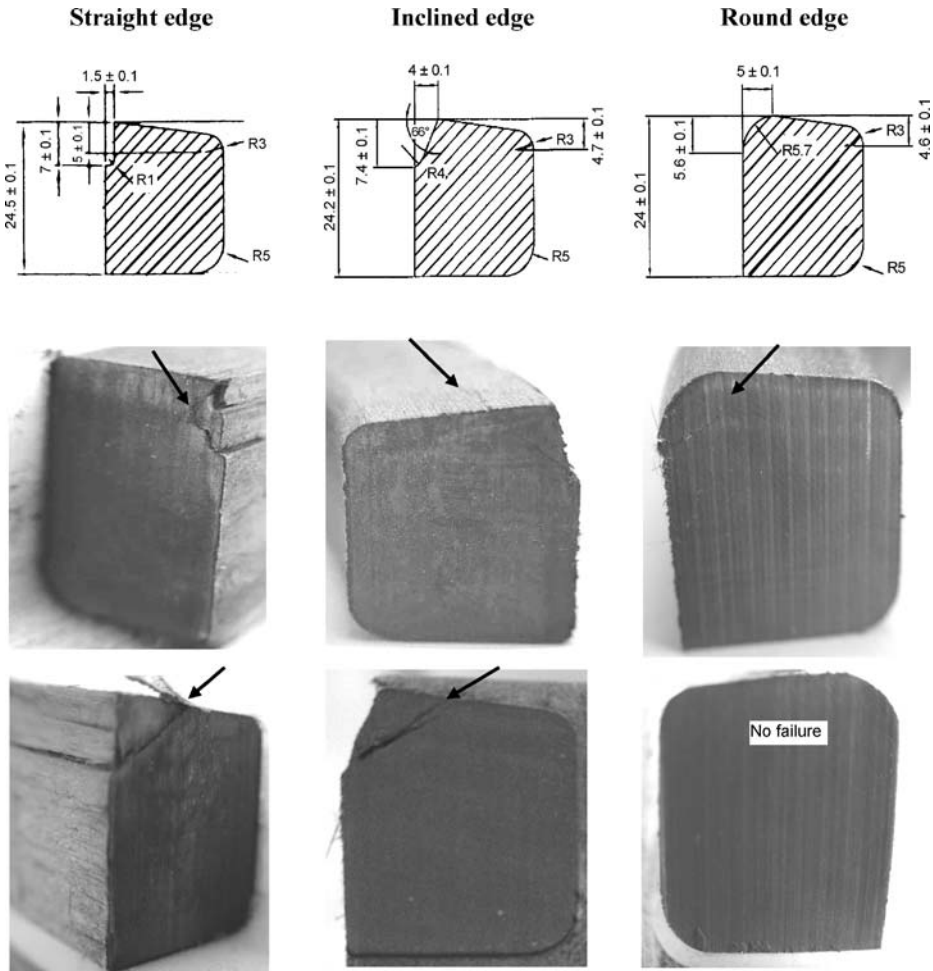


Figure 6 Cross-sectional view of different CFR-E ring geometries and failure after full-scale testing at 150 MPa.

trations by applying round edges instead of straight or inclined. As a particular case, also one static compression test on a straight edged CFR-E ring to 150 MPa did not reveal any damage. Additionally to stress concentrations, other factors such as composite composition are therefore investigated.

3.3. Full-Scale Finite Element Analysis

Stress distributions in the CFR-E ring are modelled for loading histories given in Table II, including a combination of normal loads F_z (axial) and a shear force F_x (radial). The latter is calculated from experimental results of large-scale friction (Table I) with a safety factor of 1.25 on frictional induced stresses. Under axial and shear loading, the CFR-E ring withstands high *tensile hoop* stresses σ_{YY} (along the

Table II Loading histories for full-scale finite element calculations.

Loading History	Horizontal Shear Stress at UHMWPE Surface		Finite Element Model	
	Effective Stress (MPa)	Design Stress (MPa)	Axial F_z (kN)	Radial F_x (kN)
30 MPa + $\mu = 0.21$	5.1	6.3	−1,473	309
90 MPa + $\mu = 0.09$	6.3	8.1	−4,418	398
163 MPa + $\mu = 0.0625$	7.5	10.2	−8,000	500
163 MPa + $\mu = 0.00$	0	0	−8,000	0

fibre direction), *radial compressive* stresses σ_{xx} (transverse to fibre direction), high *axial compressive* stress σ_{zz} and *radial–axial shear stress* τ_{xz} (transverse to fibre direction). As the highest shear stresses occur on a plane along 45° relative to the loading direction, these stresses are additionally modelled as the *ultimate radial–axial shear* stresses $\tau_{\max, 45}$. The maximum stresses under each loading history are summarised in Table III. Related to the functionality of the bearing elements in the ball-joint, present simulation of the CFR-E ring is rather conservative as it considers that each parameter contributing to locally higher axial load F_z (differences in local clearance, local stiffness, geometrical imperfections, ...) are assumed to coincide on the maximum loaded bearing element. Also the shear force F_x is rather conservative due to over-estimation of the axial load and applied safety factors.

Figures 7 and 8 show the respective stress distributions for the 30 and 90 MPa full-scale loading history:

- The maximum tensile hoop stresses σ_{yy} increase from 377.5 MPa (at 30 MPa loading according to running-in) towards 1,094 MPa (at 163 MPa loading according to operational conditions). For a strength in fibre direction of 2,450 MPa, the safety factor on *fibre fracture* (catastrophic failure) is higher than 2.0 in all cases. Observations in Section 3.2 show that this type of fracture was not observed in any case. It seems with increasing normal loads that a higher area of the CFR-E ring is under compressive hoop stress and a smaller part of the ring is

Table III Maximum stresses in CFR-E ring from full-scale finite element model.

Loading History	Maximum Calculated Finite Element Stresses (MPa)				
	σ_{zz} Axial Compressive	σ_{xx} Radial Compressive	σ_{yy} Tensile Hoop	τ_{xz} Radial–Axial	$\tau_{\max, 45}$
30 MPa + $\mu = 0.21$	8.07	4.24	377.5	22.6	25.0
90 MPa + $\mu = 0.09$	8.57	11.9	690.4	49.7	57.6
163 MPa + $\mu = 0.0625$	13.0	21.0	1,094	80.4	103.6
163 MPa + $\mu = 0.00$	6.4	12.1	1,036	63.4	99.2

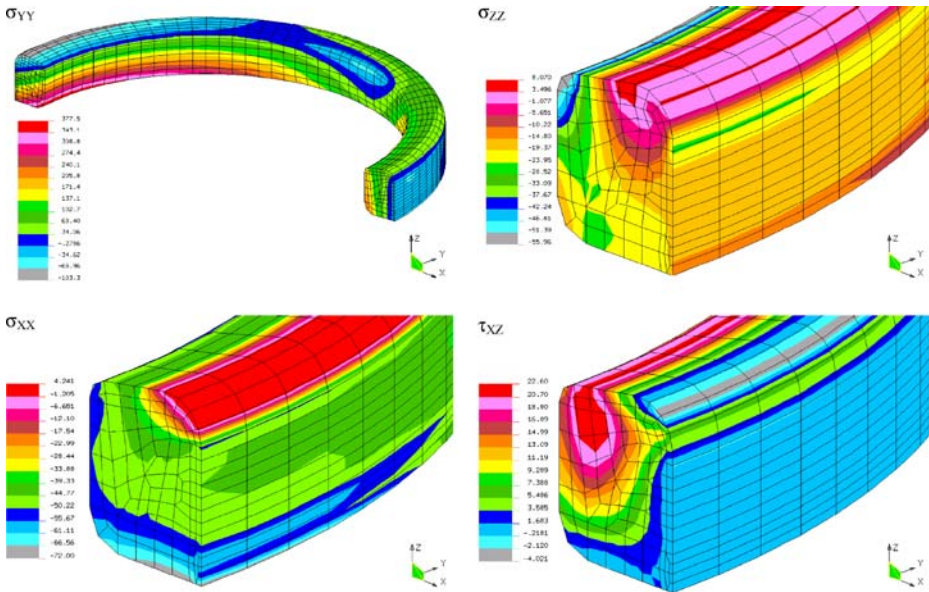


Figure 7 Stress distributions in the CFR-E ring for full-scale testing under 30 MPa + $\mu = 0.21$ (Solico BV)

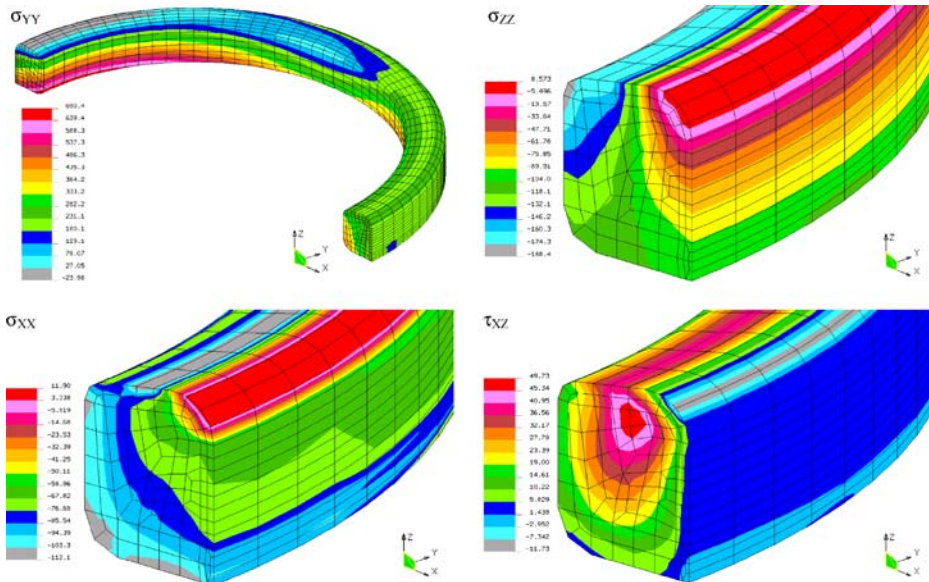


Figure 8 Stress distributions in the CFR-E ring for full-scale testing under 90 MPa + $\mu = 0.09$ (Solico BV)

consequently loaded under tensile stress, while the magnitude of compressive hoop stresses gradually diminishes. This effect is related to the retaining action of the sample holder, providing stabilisation and limitation of the radial ring deformation. According to experimental work, this retaining action was attributed to creep of the central UHMWPE part with a decrease in initial clearance between the bearing element and the sample holder [8]. Tensile hoop stresses are however not the critical factor for failure, in contrast to Kugler [15].

- The radial compressive stresses σ_{xx} are negative over nearly the entire height of the CFR-E ring, only at the machined top edge that is not retained by the sample holder, positive σ_{xx} are calculated varying between 4 MPa (under 30 MPa loading) to 21 MPa (under 163 MPa loading). Also the axial compressive stress σ_{zz} is negative over the entire height of the ring, with exception of the free top section where it is limited between 8 MPa (under 30 MPa loading) to 13 MPa (under 163 MPa loading). Pure compressive stresses are not critical for the observed failure phenomena.
- The *radial-axial* shear stress τ_{xz} attains maximum 22 MPa (at 30 MPa normal load) and increases towards 80 MPa (at 163 MPa normal load). Within a cross-section of the CFR-E ring under maximum normal load, it reveals that the transverse shear stress is reasonably low for zones without compressive stresses σ_{xx} and σ_{zz} , while it is considerably higher for zones subjected to compressive σ_{xx} and σ_{yy} , rising towards 80 MPa. From literature [17] it is known that the presence of a hydrostatic stress distribution increases the strength of a composite material and allows for higher shear stresses without fracture. Present hydrostatic stresses are induced by the compressive loading of a visco-elastic material into a resistant steel holder: with a radial pressure on the inside of the CFR-E ring of approximately 140 MPa under 150 MPa full-scale loading of the bearing element, the ring hypothetically acts as the wall of a pressure vessel at 1,400 bar possibly increasing towards 3,000 bar under full loading capacity. It is clear that a maximum shear stress is located just beneath the outer surface of the CFR-E ring, causing a strong stress variation from the machined edge towards the bulk of the CFR-E ring. The zone of maximum shear stress seems elliptical and elongates towards the top surface of the CFR-E ring. Moreover, the stress-gradient is oriented along 45° relative to the machined edge and its shape shows good correspondence with the orientation and propagation of experimental fractures after large-scale static loading (Figure 6). Corresponding to fracture aspects in Figure 6, the radial-axial shear stress τ_{xz} is the most critical parameter for avoiding *shear failure*. Therefore, it is the objective to obtain a safety factor of at least 1.2 with respect to the ultimate shear strength $\tau_{\max, 45^\circ}$. Its distribution is simulated in Figure 9 for various loading histories, where a critical value of 33 MPa under non-hydrostatic conditions and 104 MPa under hydrostatic conditions is required under maximum loading conditions. This criterion for radial-axial shear stress will be used as input for small-scale UC and SBS tests for determination of a representative shear failure criterion.

Effects of friction at the UHMWPE surface on the stress distribution in the CFR-E ring at 163 MPa normal contact pressure is illustrated in Figure 10 for a coefficient of friction $\mu = 0.0625$ and $\mu = 0$. The maximum radial hoop stress σ_{yy} (not shown) decreases from 1,094 towards 1,036 MPa and is still located at the bottom edge of

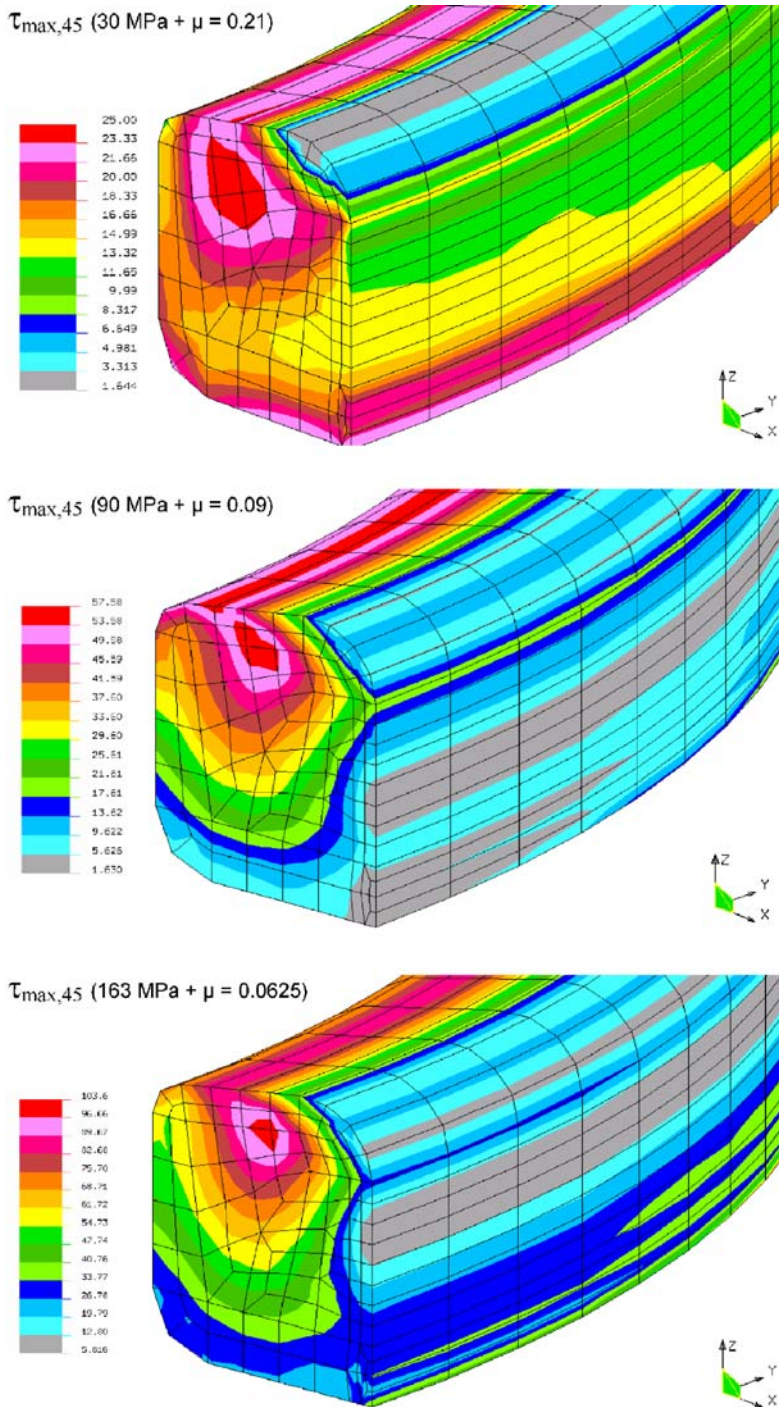


Figure 9 Ultimate shear stress in the CFR-E ring for full-scale testing under different loading histories (Solico BV)

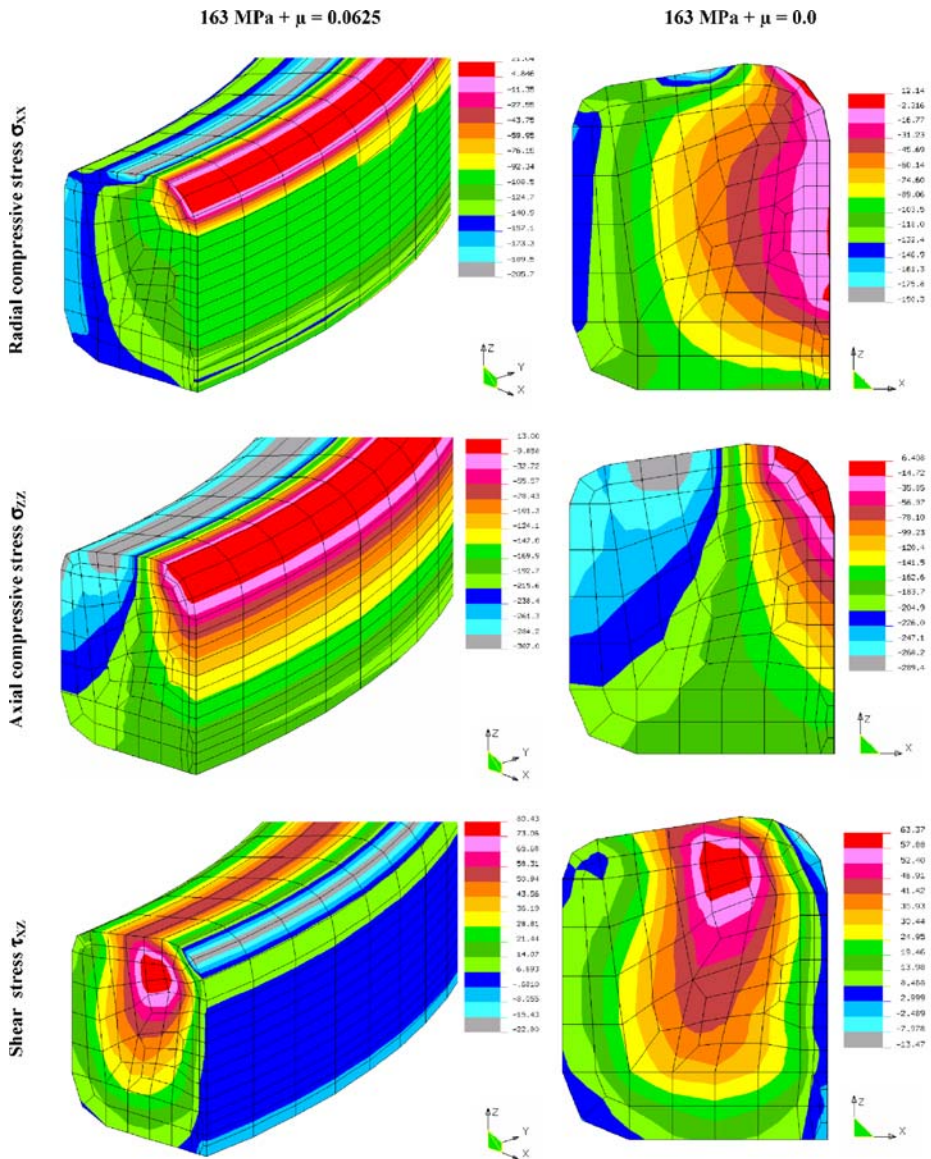


Figure 10 Influence of friction at the UHMWPE surface on stress distribution in the CFR-E ring for full-scale testing under 163 MPa (Solico BV)

the CFR-E ring in contact with the UHMWPE disc. Contrarily, the minimum hoop stress of 36 MPa on top of the ring in case of friction increases towards 60 MPa under pure static conditions. The absolute radial compressive stresses σ_{xx} and axial compressive stresses σ_{zz} are lower in absence of friction (approximately one half) and its decrease over the edge of the ring and towards the centre of the ring is less steep. The shape of the radial-axial τ_{xz} shear stress distribution is comparable,

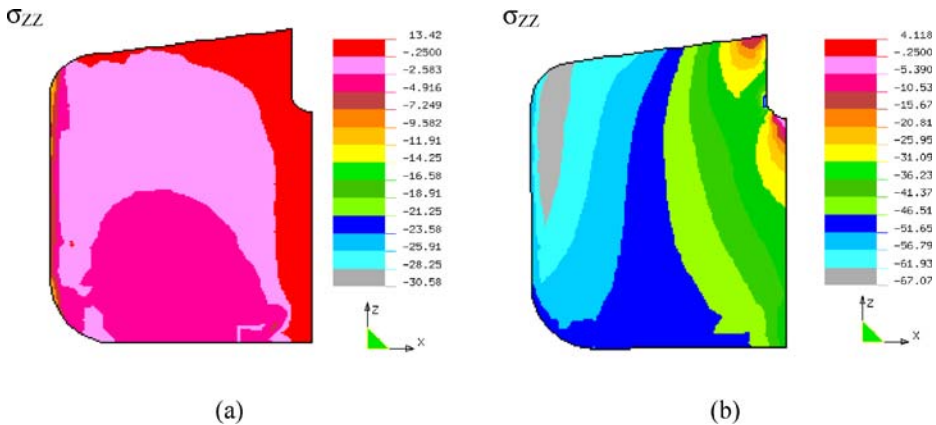


Figure 11 Influence of ring geometry with stress concentrations on straight edged CFR-E rings for full-scale testing under (a) 15 MPa + $\mu = 0.0$, (b) 60 MPa + $\mu = 0.0$ (Solico BV)

although its maximum value decreases from 80 to 63 MPa. When friction is not assumed, the hydrostatic stress component is consequently lower with also a reduction in critical ultimate shear strength from 104 to 99 MPa.

Stress concentrations on a CFR-E ring with a straight edge geometry are shown in Figure 11 for a coefficient of friction $\mu = 0$. Critical situations occur mainly under low static loading conditions (15 to 50 MPa), inducing an inhomogeneous distribution of axial compressive stresses σ_{zz} over the ring edge. There is a concentration of tensile and compressive stresses near the machined edge, varying between 13 MPa (under 15 MPa) or 4 to -36 MPa (under 50 MPa) over a short distance. Tensile stresses are attributed to the indentation of the ball counterface in the centre of the polymer disc and disappear as the normal load increases towards an overall compressive stress state. Compared to the previously discussed round edged CFR-E rings as applied in the final design, this complex stress situation is converted into a gradual decrease of stresses over the ring edge.

4. Small-Scale Test Results

4.1. Short Beam Shear Tests (SBS)

In design of an appropriate characterisation test for shear failure of finished CFR-E rings (i.e., machined with fillets as shown in Figure 6), three comparative tests are performed on (1) ring geometries according to ASTM standards (thickness 6 mm, width 24 mm, span 24 mm), (2) rectangular section rings (thickness 20 mm, width 30 mm, span 80 mm) and (3) finished or machined section rings (thickness 20 mm, width 24 mm, span 80 mm). The latter is not assumed as an absolute measurement of the ILSS but in correlation to previous full-scale tests, it should be used as a relative qualification test. For a final round-edged CFR-E ring, it is verified that the *radial–tangential* shear stress τ_{xy} varies, respectively, (1) between 67 to 69 MPa (12.7 to 12.8 kN) according to ASTM standards, (2) between 51 and 54 MPa (32.7 to 34.6 kN) on rectangular section rings and (3) between 48 and 50 MPa (30.5 to

31.1 kN) on finished ring geometries. It is clear that a fit-to-purpose test (*the Maeslant test*) on real sample geometries is presently required for evaluation of the CFR-E ring strength, as standardised methods would imply an over-estimation of the strength capacity while eventual stress concentrations as modelled below are introduced on finished section rings. Concerning the discussion whether the ring segment should be loaded convexly or concavely, it is verified that the concave geometry provides an *radial-tangential* shear stress τ_{XY} that is 1.4 times higher than the convex geometry. In correspondence to the ASTM standard and safety design rules, load is applied on the outer ring radius of a convex geometry.

For the different CFR-E ring geometries and in parallel to the improvement of the composite properties as illustrated in the discussion part, there is noted a steady increase in maximum SBS loading capacity from 17 kN (initial straight edged ring geometry) towards 18 kN (inclined edge geometry) and finally attaining 20.7 to 31.1 kN (round edge geometry), representing a *radial-tangential* shear stress τ_{XY} increasing from originally 15 to 18 MPa towards 34.3 MPa and finally 50 to 52 MPa. For a ring segment submersed for 100 h in Tellus 22 oil before testing, there is a reduction in τ_{XY} from 52 to 49 MPa, possibly due to reaction between the oil and the epoxy matrix constituent. The variation in τ_{XY} measured on three separate segments from one production batch decreased from initially 10% towards 4.2%. It was visually ascertained on both a cross-section and top view (Figure 12) that each sample failed by interlaminar shear.

From a hypthetic finite element calculation on a standard ASTM beam loaded at 2 kN, it reveals that the compressive stresses σ_{XX} (corresponding to the radial compressive stress in full-scale tests), σ_{YY} (corresponding to the tensile hoop stress in full-scale tests) and σ_{ZZ} (corresponding to the axial compressive stresses in full-

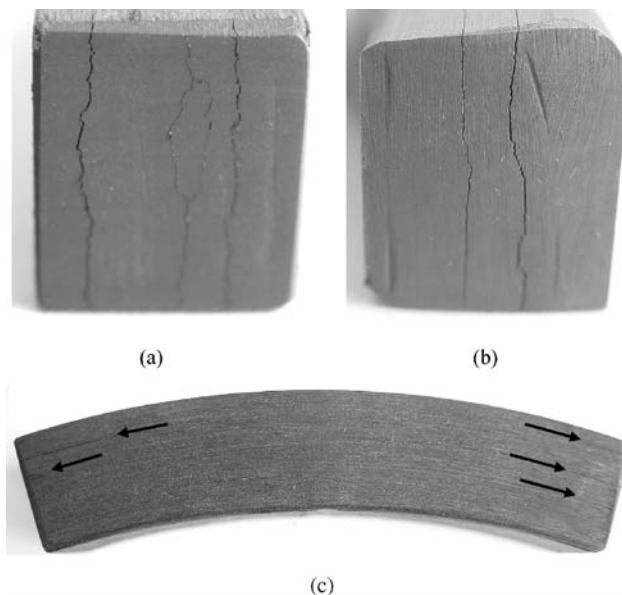


Figure 12 Macroscopic fracture aspect of CFR-E rings with different test geometry after small-scale SBS-test (a) standard geometry cross-section view, (b) round edged cross-section view, (c) round edged top view (*Maeslant-test*)

scale tests) located at the supporting points, respectively, attain -55 , -240 and -25 MPa with a corresponding *radial–tangential* shear stress $\tau_{XY} = 20$ to 27 MPa under the loading pin. Hydrostatic stress conditions only occur near those supporting points, as in the centre of the beam between the supporting points $\sigma_{XX} = 2$ MPa, $\sigma_{YY} = 75$ MPa and $\sigma_{ZZ} = 8$ MPa with a corresponding *radial–tangential* shear stress $\tau_{XY} = 3$ MPa. It is concluded from this preliminary simulation that the stress situation in the centre of the beam is the most critical and will be used as a further design criterion (see discussion part 5.1).

The effect on the *radial–tangential* shear stress (τ_{XY}) of additional stress concentrations own to the real CFR-E ring geometry and its specific radius of curvature are calculated in Figure 13 for a half beam under 27 kN normal load. Both the outer beam geometry and a section cut along the vertical plane perpendicular to the loading pin are presented. Local concentrations at the supporting points rise to $\tau_{XY} = 50.0$ MPa, while $\tau_{XY} = 43.3$ MPa in the centre of the beam as calculated from a detailed cut between the load supporting points. The distribution of the *radial–tangential* shear stress τ_{XY} over the sample thickness (parallel XZ-cut) as taken at a quarter distance of the span (between pin and supporting point) is shown in Figure 14 for a 27 kN normal load, with the influence of the machined ring edge and local stress concentrations. There is a sharp variation in *radial–tangential* shear stress τ_{XY} between 0 and 30 MPa over the ring edge. The variation of the *radial–tangential* shear stress τ_{XY} over the radial thickness of the CFR-E ring with inner radius 104.5 mm and outer radius 124.5 mm is studied from three cut sections (parallel XY-cut) at radii 109.5, 112.5 and 114.5 mm. From calculations in each section, the maximum ILSS equals 62.5, 48.0 and 43.3 MPa, respectively, under 27 kN normal load. However, the shear stress distribution is not symmetrically with respect to the vertical plane cut nor through the entire sample thickness due to local stress concentrations near the loading supports and present ring geometry. It is

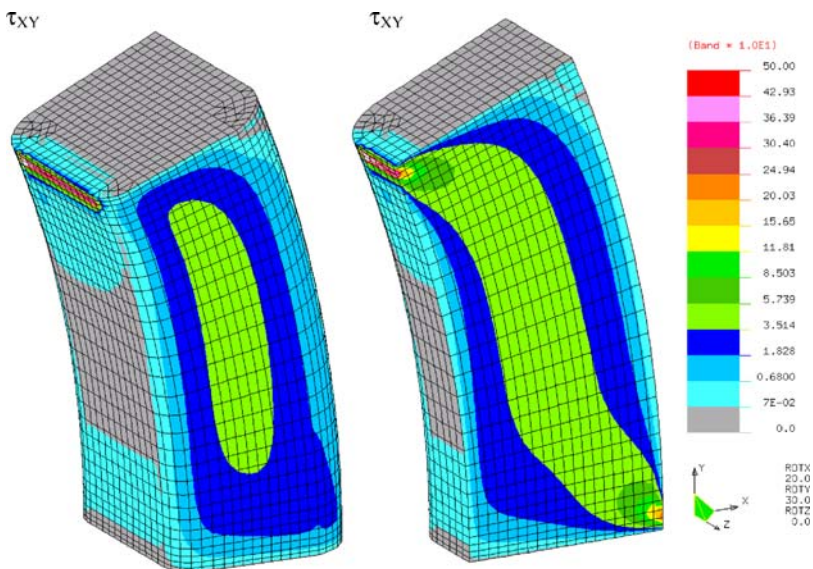


Figure 13 Distribution of radial–tangential shear stress over a half beam in a small-scale *SBS-test* (*Maeslant test*) under 27 kN (Solico BV)

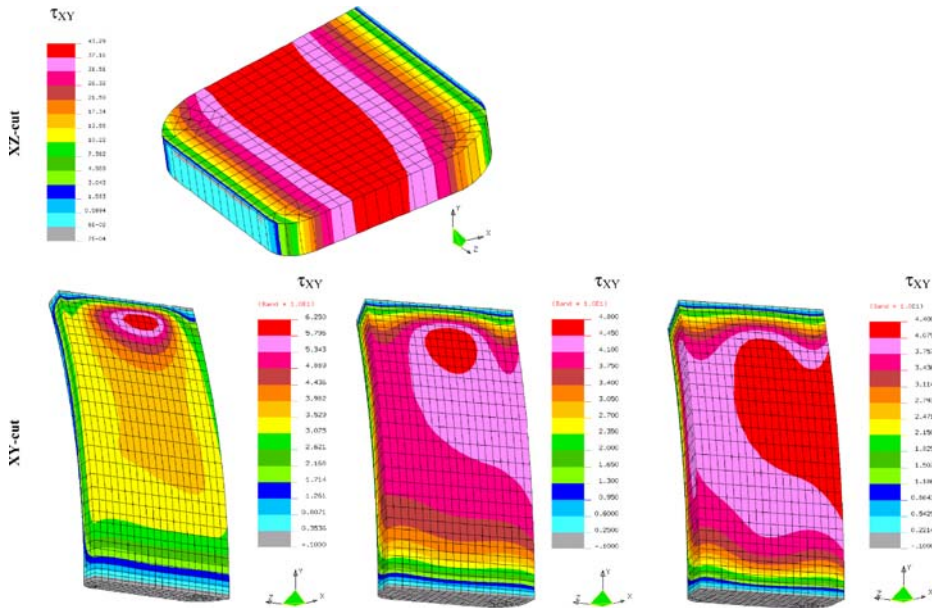


Figure 14 Distributions of radial–tangential shear stress over XZ-cuts and XY-cuts in a small-scale SBS-test (*Maeslant-test*) under 27 kN

demonstrated that those stress distributions influence the strength measured in present *Maeslant test*.

Compared to the ASTM calculation of the *radial–tangential* shear stress τ_{XY} for the *Maeslant test* geometry with a ring outer radius 124.5 mm, inner radius 104.5 mm, thickness 20 mm and width 24 mm (the cross-section then equals 453 mm²) with a span 80 mm, the *radial–tangential* shear stress $\tau_{XY} = 44.7$ MPa under 27 kN. These values are in very good correspondence with the reported finite element simulation of $\tau_{XY} = 43.3$ MPa (27 kN) as global value, serving as validation of previous models. Small deviations (ASTM shear stress calculations are 3% to 4% lower) are attributed to anisotropy and fillet geometries. For a smaller outer radius of 248.5 mm (cross-section then equals 447 mm²), the calculated $\tau_{XY} = 45.3$ MPa. Therefore, the influence of eventual machining tolerances on the apparent shear strength and deformation of the CFR-E ring should be carefully considered as also reported in correlation to experimental experience on static loading of full-scale bearing elements [8].

4.2. Uniaxial Compression Tests (UC)

Contrasting to the *SBS-test* that takes into account the CFR-E ring geometry, present *UC test* is a pure material characterisation tests performed on a square cross-section. Although, test results for the maximum compressive force show a consistent evolution in parallel to the different CFR-E ring geometries that were shown in Figure 6, ranging from 17 kN (initial straight edged ring geometry) towards 20 kN (inclined edge geometry) and 44 kN (final round edge geometry) corre-

sponding to, respectively, $\sigma_{\max} = 90, 104$ and 144 MPa compressive strength (formula (2)), taking into account the effective sample area. The variation of compressive strength on three separate segments from one ring was, respectively, 12%, 6% and 1.3%. The progressive increase in strength with ongoing design of the reinforcing CFR-E ring will be evaluated in Section 5.2. The fracture aspect after failure at maximum load is shown in Figure 15 and looks very similar to the *radial-axial* shear mode failure observed after full-scale testing, with crack propagation under nearly 45° to 60° shear angles. No transverse cracks resulting from buckling were observed. As CFR-E bulk material is presently loaded, crack initiation is not induced by eventual stress concentrations at the machined CFR-E ring edges. Possible stress concentrations during a *UC* test and the estimation of *radial-axial* shear strength from experimental compression strengths requires further FEM analysis.

Figure 16 shows the finite element calculations for the *tensile hoop* stress σ_{YY} , the *axial compressive* stress σ_{ZZ} , the *radial compressive* stress σ_{XX} and the *radial-axial* shear strength τ_{XZ} varying over the semi-thickness of a CFR-E ring segment that is loaded under 98 MPa normal contact pressure (20 kN). Friction between the sample top surface and the compression plate is translated into a fixation of the nodes on the top surface (no lateral contraction is allowed), resulting in very high stresses appearing at the corners of the specimen in contact with the upper compression plate. The influence of the compression plate roughness was incorporated into the frictional conditions. The compressive σ_{XX} , σ_{YY} and σ_{ZZ} stresses attain $-146, -147$ and -280 MPa in those corners inducing a *hydrostatic stress* state. In the centre of the specimen, the principal compressive stresses σ_{XX} and σ_{YY} nearly disappear or become slightly positive and solely an overall axial compressive stress $\sigma_{ZZ} = -98$ MPa occurs. Due to edge effects, σ_{ZZ} is -80 MPa near the borders of the specimen, but remains negative. The radial compressive stress varies parabolically over the radial (X) direction near the top surface and is equalised in the centre of the specimen. The *radial-axial* shear stress τ_{XZ} at the top surface is nearly symmetric relatively to the centre of the top surface, as a reaction to lateral displacement in contact with the compression plates: At one edge it attains 80 MPa, at the opposite side it has -70 MPa. Small discrepancies in symmetry are attributed to the specific sample geometry. The τ_{YZ} shear stresses only govern on the top surface and range between 4 and -16 MPa (not shown). Most important for shear failure under small-scale *UC*-testing are the *ultimate radial-axial shear*

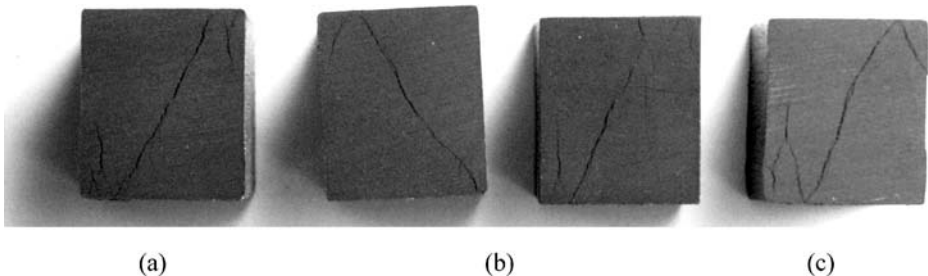


Figure 15 Macroscopic fracture aspect of CFR-E rings with different initial geometry after small-scale *UC*-test with different compressive strength (a) straight edged (90 MPa), (b) inclined edged (104 MPa), (c) round edged (144 MPa)

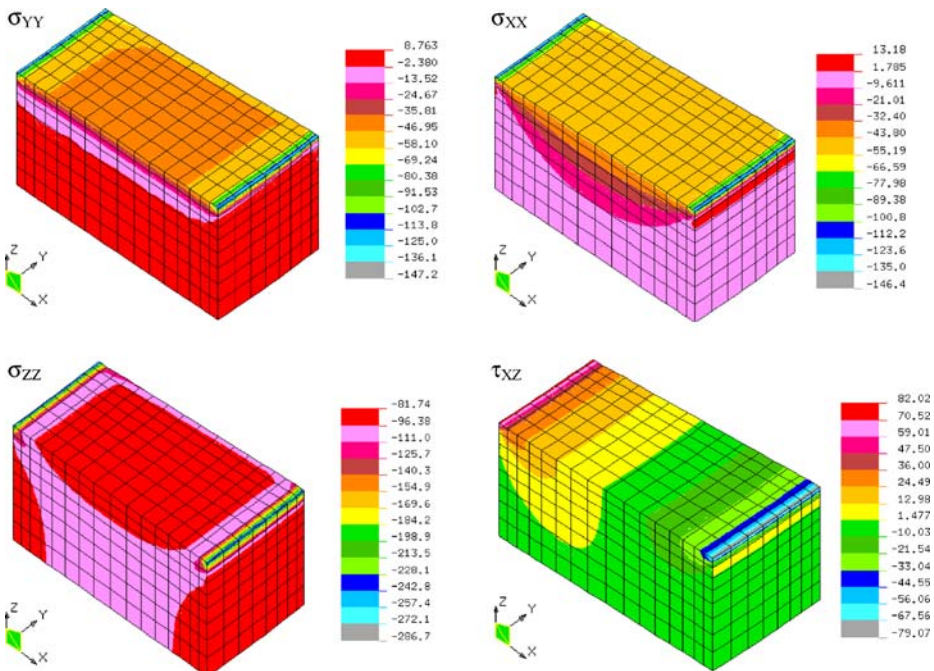


Figure 16 Stress distribution in a CFR-E ring segment for small-scale *UC-tests* with fixed contact surface under 20 kN or 98 MPa (Solico BV)

stresses $\tau_{\max, 45}$ under 45° relative to the loading direction, given in Figure 17. Under hydrostatic conditions near the corners of the sample, high shear stresses up to 107 MPa occur. These serve as initiation for fracture as experimentally observed near the edges of the cubic samples and propagation under 60° (Figure 15). Meanwhile in the central zone, the ultimate shear stress is about 46 MPa, corresponding very well

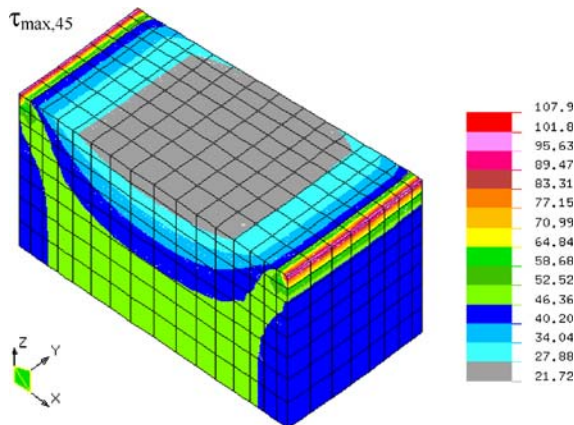


Figure 17 Ultimate radial–axial shear stress for small-scale *UC-tests* with fixed contact surface under 20 kN or 98 MPa (Solico BV)

with half the measured compressive stress of 98 MPa. Therefore, the critical *radial-axial* shear stress can be estimated from the load at failure in a *UC-test* and is representative for the parts of the CFR-E ring not subjected to a hydrostatic state of stress, being the most critical stress condition for full-scale fracture.

The gradual build-up of normal stresses and *radial-axial* shear stresses in the CFR-E bulk and creation of hydrostatic (near the corners) and non-hydrostatic stress (in the centre) conditions is attributed to friction between the CFR-E sample surface and the compression plate. Under sliding contact between top CFR-E surface and compression plate (i.e., zero friction) there is a nearly homogeneous and very small compressive stress $\sigma_{XX} = 0$ to -1 MPa and $\sigma_{YY} = 0$ to -1 MPa through the entire bulk with consequently a constant axial compressive stress $\sigma_{ZZ} = -98$ MPa. Consequently, the *ultimate radial-axial* shear stress remains constant over the entire CFR-E bulk and is not useful in a predictive failure criterion for a CFR-E segment. The real friction coefficient of the CFR-E ring segment in contact with a steel plate is implemented from a full-scale sliding test on bearing elements without polymer lip and direct contact between CFR-E ring and its counterface [16]. For 150 MPa contact pressure, $\mu_s = 0.11$ (static coefficient of friction) and $\mu_d = 0.07$ (dynamic coefficient of friction), which is significantly higher than friction of UHMWPE surfaces from Table I. From extrapolation, a coefficient of friction $\mu_d = 0.10$ should be applied for modelling under 98 MPa. These sliding conditions were however not practically developed because of unacceptable high friction and severe abrasive counterface wear.

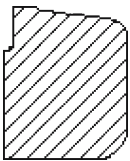
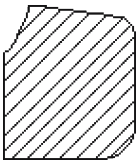
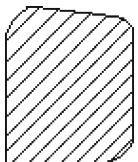
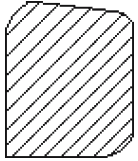

5. Discussion

From presented experimental results and finite element simulations, the stress distributions in the CFR-E ring under full- and small-scale testing are known. It is demonstrated that a *radial-tangential* shear stress τ_{XY} can be estimated from *SBS-tests* on real sample geometries and its value is in accordance with calculations from ASTM standards. A *radial-axial* shear stress can be estimated from half the compressive stress in a *UC-test*. A summary of the respective shear stresses are given in Table IV in parallel to the different ring geometries applied during the design process. The calculated strength of the CFR-E ring should now be translated into a representative failure criterion and an optimisation process that avoids fracture under full-scale loading.

5.1. Interpretation of Various Testing Methods and Small-Scale Failure Criterion

Fracture of present bearing geometries is determined by *radial-axial* shear stresses τ_{XZ} according to Figures 6 and 9. This stress is directly determined from a small-scale *UC-test*, although not favourable to be performed due to high cost. Based on small-scale *SBS-tests*, a representative *radial-tangential* shear stress failure criterion will therefore be determined. For CFR-E rings with identical geometry, composition and production quality, the experimental difference between *radial-axial* and *radial-tangential* shear strength is shown in Table IV: for a $\tau_{XZ} = 71$ to 72 MPa from a *UC-test*, only a $\tau_{XY} = 48$ to 50 MPa is measured on a *SBS-test*. The fact $\tau_{XY} < \tau_{XZ}$ can be intuitively related to the influence of the unidirectional fibre reinforcement ‘propagation path,’ which is impeded in radial direction. Moreover, the

Table IV Evaluation of full-scale fracture, small-scale shear stress and composite composition.

CFR-E Ring Geometry	Full- Scale Fracture at 150 MPa	UC-Test Strength		SBS-Test Strength		Composition			
		Max Load (MPa)	τ_{XZ} (MPa)	Max Load (kN)	τ_{XY} (MPa)	Density (g/cm ³)	Fibre (%)	Porosity (%)	Resin (%)
	Yes	86	43	17	26	1.537	69	3.5	27.5
Resin A 	Yes	104	52	18	28	1.546	67	1.9	31.1
Resin A 	Yes (50%) No (50%)	Not performed*		20	31	1.542	66	1.5	32.5
Prototype I Resin A 	No	Not performed*		29	47	1.534	60	<1.4	38.6
Prototype II Resin A 	No	144	72	30 31	49 52	1.591 1.574	64 64	1.5 0.4	34.5 35.6
Prototype I Resin B									

*Only limited tests due to expensive cost and difficulties in sample preparation.

low *radial–tangential* shear strength is attributed to the positive stresses σ_{XX} (rising towards 13 MPa) between the load supports and asymmetric stress distribution under *SBS-test*, which are implied by the specific ring geometry. Under *UC-tests*, a negative σ_{ZZ} and more symmetric stress distribution for σ_{XX} , σ_{YY} (Figure 16) is translated into a higher *radial–axial* shear stress. Shear failure of a CFR-E ring segment loaded in a *SBS-test* is the most critical and it is more suitable for sample preparation compared to *UC-tests*.

Correlated to failure in full-scale tests there appears a critical SBS normal load at 20 kN limiting the failure/non-failure behaviour, corresponding to $\tau_{XY} = 31$ MPa (Table IV). Including a safety factor 1.3 on *radial–tangential* shear failure, based on safe-engineering experience, a final normal load of 27 kN on *SBS-tests* is demanded, corresponding to 42.5 MPa *radial–tangential* shear stress and 63 MPa *radial–axial* shear stress in critical zones not subjected to a hydrostatic stress state. These situations were simulated in Figure 14 (SBS) and Figure 17 (UC). This small-scale failure criterion for a *Maeslant-test* is adequately related to the stress distribution in full-scale testing: concerning the maximum allowable shear stress $\tau_{\max, 45}$ in the full-scale design under maximum loading conditions (163 MPa + $\mu = 0.0625$), there are noticed non-hydrostatic stresses near the machined edges of the CFR-E ring with positive σ_{XX} and σ_{ZZ} (Figure 10), where it is calculated that the *radial–axial* shear stress attains 33 MPa (Figure 9). As it was additionally verified on a full-scale static loading experiment under 180 MPa contact pressure that no failure of a CFR-E ring occurred [8] while the required strength in a *Maeslant-test* is 27 kN, this implies a safety factor on *radial–axial* shear failure of two on full-scale shear fracture.

As such, it is demonstrated that a combination of numerical stress analysis and evaluation of experimental test results was successful in reducing the CFR-E ring fracture (e.g., see final cross-section in Figure 6) and lead to the design of a representative small-scale failure criterion. Performing a good designed *SBS-test* (*Maeslant-test*) implies the ease of handling test samples against acceptable economic cost and delivery time. However, it is crucial that the original machined sample geometry is carefully considered, inducing a characteristic stress condition. Therefore, also other techniques for compression testing of composite rings as proposed by e.g., Chaudhuri et al. [18] or Joyce [19] are presently not applicable: the tests, mainly designed for thin rings, have a uniform stress distribution in hoop and radial direction and no loading in axial direction. Pressurized ring tests for composite pressure vessel hoop strength and stiffness [20] also not apply: In this process it is assumed that the ring collapses when the first hoop (inner-most hoop) ply fails. Kugler et al. [15] proposed an axial loading method for thick rings (up to 140 mm internal diameter and 38 mm thick), with radial inward expansion due to the Poisson effect leading to radial compressive stresses. This stress state implies a hydrostatic radial pressure on the outside of the composite ring, with 500 to 600 MPa hoop stress and 90 to 140 MPa radial stress at failure for carbon fibre/polysulfone rings. The observed fracture with initiation at the outer diameter and propagation through the entire ring thickness in radial direction was however different from present failure mode.

5.2. Optimisation of Composite Geometry and Production Parameters

One action in reducing shear failure and increasing the shear strength of the CFR-E composite rings is the improvement of the edge geometry from the original straight

edge towards round edge. It was illustrated by finite element calculations that stress concentrations near the machined edge are reduced and show a progressive circumferential stress variation.

In Table IV, the variation in strength of the CFR-E ring is also studied in parallel to the composite composition and production process. Density measurements are done in accordance to ISO 1183-1987 or ASTM D792-66: “Standard test methods for specific gravity and density of plastics,” with weight measurements of a CFR-E sample before and after immersion in distilled water (precision 0.5 mg). The porosity content was calculated (methods for direct experimental determination are not available) from density measurements with known volumetric mass of epoxy resin and from carbon fibre volume fractions. For both ‘Resin A’ and ‘Resin B’ a different volumetric mass of, respectively, 1.090 and 1.175 g/cm³ is used. The fibre volume content was determined from ASTM D3171-99: “Standard test methods for constituent content of composite materials” where the epoxy matrix digestion is done in 70% nitric acid (digestion in standard sulphuric acid was incomplete). Preliminary measurements are performed on an inner, middle and outer part of the ring section, revealing very small variations. As this indicates homogeneity over the full ring section, a representative sample is taken from the ring section and split into parts for better digestion. The average value of three measurements is taken as density or fibre volume content. The weight of a CFR-E ring specimen is 15 to 20 g.

For the initial batch of wound CFR-E rings with straight edged geometry, a very high fibre volume content (69%) is measured with consequently relatively low resin percentage. Moreover, the values measured on samples of identically processed CFR-E rings showed high variation in composition, $\pm 3\%$. It is known that high fibre volume fractions result in high stress concentrations in the matrix and thus lower transverse shear strength from UC-tests and SBS-tests. According to Hull and Clyne [21], there is a strong relation between the strain magnification in the fibre/matrix interface and the fibre volume fraction. Due to better control of the original processing parameters (i.e., winding speed and fibre tension during winding) and curing conditions (curing temperature and time) the initially very high porosity ($3.5\% \pm 3\%$) could be reduced towards 1.5% with a reduction in fibre content from 69% to 66% in the first prototype I ring. This results in an increased *radial-axial* shear strength on UC-tests from 43 to 52 MPa (21% higher), while the increase in *radial-tangential* shear stress on SBS-tests is 26 to 28 MPa (only 8% higher). This again illustrates the combined effect of geometry and composition on the shear strength measurements and the difference $\tau_{XY} < \tau_{XZ}$. More details on the relation between winding parameters and the ILSS were known from investigations by Cohen [22] or Zhao [23]. However, the composition of the prototype I/resin A ring was not suitable for a reduction in full-scale failure and further improvement was achieved by application of different processing conditions and identical resin (prototype II/resin A ring) or by application of a new epoxy resin formulation under original processing conditions (prototype I/resin B ring). Both solutions were satisfying with a SBS-test normal load of 29 to 31 kN, which is well above the 27 kN limit. Other improvements of the ILSS and fibre-matrix bonding consist of small size matrix texturing as proposed by Blanco et al. [4] with different binder types and/or curing cycle controlling the shrinkage. Also different fibre treatments as done by Li [24] increase the ILSS, although less economically and time-consuming for present purpose. There is also a reported risk that stronger interface bonding possibly changes failure from shear mode into catastrophic.

Present filament winding process is preferred above laminated carbon/epoxy as investigated by Chaudhurri [18] as formation of kink bands and shear-crippling failure is observed under hydrostatic compression. Finally, an on-the-field test of five hundred reinforced polymer bearing elements according to prototype I or II are incorporated in the Maeslant ball-joint and did not reveal any fracture.

From Table IV and previous discussion, it was finally assumed that fibre percentages should be between 58% to 63%, with porosities below 2.5% and an epoxy resin content above 34.5%. Consequently, the ring has a mass between 475 to 510 g. Higher fibre content and lower resin content leads to failure: It could be visually observed from the CFR-E rings (Figure 5(a)) that the fractured rings with original composition have a 'dry' aspect relatively to the 'wet' aspect of the unfailed rings in Figure 6. According to Costa et al. [25] carbon/fibre epoxy composites have typical higher void contents compared to other resins for the same manufacturing procedure (between 5.6% to 1.5%) and ILSS between 55 and 71 MPa for fabric laminates. Cracks typically initiated at triangular shaped voids.

6. Conclusions

Fracture of a carbon fibre/epoxy (CFR-E) reinforcing ring was observed after full-scale loading of a bearing element to 150 MPa, initiating near the machined edge. From finite element analysis, a non-hydrostatic stress state is determined in this zone with governing radial–axial shear stresses of 33 MPa. In the bulk of the ring, hydrostatic stresses allow for higher shear stresses up to 104 MPa. The former non-hydrostatic stress state is however the most critical for failure and a small-scale design criterion was successfully defined for qualifying the composite shear strength. Although the radial–axial shear strength is crucial for the full-scale geometry, it was translated into a radial–tangential fracture criterion from a short-beam-shear testing on the real ring geometry. The radial–tangential shear strength is lower than radial–axial shear strength from a uniaxial compression test, as additional stress concentrations should be taken into account. There is good consistency that composites with lower shear strength resulted in full-scale failure, while higher shear strengths corresponding to 27 kN normal loads showed no failure. The increase in shear strength was attained by changing straight edges into round edge geometries and close control of the production process with reduction in fibre content (<64%) and low porosity content (<2.5%). Besides a favourable composition of the composite, an additional fit-to-purpose qualification on the final ring geometry is required for avoiding failure.

Acknowledgements The authors of Ghent University appreciate the cooperation with the Nederlandse Rijkswaterstaat for deliverance of test specimen and to be involved in the re-design of the Maeslant storm surge barrier. Solico BV is greatly acknowledged for the performance of finite element modelling and allowance to publish test results. Many thanks to Ludo and Han for their help and useful discussions!

References

1. Leendertz, J.S., Van Schepdael, L., Van Paepegem, W., Samyn, P., De Baets, P., Degriek, J.: Änderung der gelenklagerkonstruktion des sturmflutsperrwerks bei rotterdam. Stahlbau 75, 45–54 (2006)

2. Liu, H.S., Tai, N.H., Chen, C.C.: Compression strength of concrete columns reinforced by non-adhesive filament wound hybrid composites. *Composites* **A31**, 221–233 (2000)
3. Kelly, G., Hallström, S.: Strength and failure mechanisms of composite laminates subject to localised transverse loading. *Compos. Struct.* **69**, 301–314 (2005)
4. Blanco, C., Casal, E., Granda, M., Menendez, R.: Influence of fibre-matrix interface on the fracture behaviour of carbon–carbon composites. *J. Eur. Ceram. Soc.* **23**, 2857–2866 (2003)
5. Li, M., Matsuyama, R., Sakai, M.: Interlaminar shear strength of C/C-composites: the dependence on test methods. *Carbon* **37**, 1749–1757 (1999)
6. Kedward, K.T.: On the short beam test method. *Fibre Sci. Technol.* **5**, 85–95 (1972)
7. Sawyer, J.W.: Investigation of test technique for measuring shear strength of two-dimensional carbon–carbon composites. NASA Report No. TM 100647, (1988)
8. Samyn, P., Van Schepdael, L., Leendertz, J.S., Van Paepegem, W., De Baets, P., Degrieck, J.: Deformation of reinforced polymer bearing elements on full-scale compressive strength and creep tests under yielding conditions. *Polym. Test.*, **25**, 230–245 (2006)
9. Samyn, P., Van Schepdael, L., Leendertz, J.S., Gerber, A., Van Paepegem, W., De Baets, P., Degrieck, J.: Large-scale friction and wear tests on a hybrid UHMWPE-pad/Primer coating combination used as bearing element in an extremely high-loaded ball-joint. *Tribol. Int.* **39**, 796–811 (2006)
10. Ticona GmbH: Ultra high molecular weight polyethylene: Product Catalogue GUR, pp. 4–7 (2002)
11. Liu, H.S., Liao, W.C., Tseng, L., Lee, W.H., Sawada, Y.: Compression strength of pre-damaged concrete cylinders reinforced by non-adhesive filament wound composites. *Composites* **A35**, 281–292 (2004)
12. Xie, M., Adams, D.F.: Study of three- and four-point shear testing of unidirectional composite materials. *Composites* **26**, 653–659 (1995)
13. Cui, W.C., Wisnom, M.R.: Contact finite element analysis of three- and four-point short beam bending of unidirectional composites. *Compos. Sci. Technol.* **45**, 323–334 (1992)
14. Pahr, D.H., Rammerstorfer, F.G., Rozenkrans, P., Humer, K., Weber, H.W.: A study of short-beam-shear and double lap shear specimens of glass fabric/epoxy composites. *Composites* **B33**, 125–132 (2002)
15. Kugler, D., Moon, T.G.: A technique for compression testing of composite rings. *Composites* **A33**, 507–514 (2002)
16. Samyn, P., De Baets, P., Van Paepegem, W., Van Schepdael, L., Suister, E., Leendertz, J.S.: Design of a carbon/epoxy reinforcing ring reducing creep of UHMWPE in high-loaded sliding contacts. In: Kozma, M. (ed.) 8th International Conference on Tribology, pp. 89–96. Veszprem (2004)
17. Hine, P., Duckett, R.A., Kaddour, A.S., Hinton, M.J., Wells, G.M.: The effect of hydrostatic pressure on the mechanical properties of glass fibre/epoxy unidirectional composites. *Composites* **A36**, 279–289 (2005)
18. Chaudhuri, R.A., Kim, D.: Localization and shear-crippling (kinkband) instability in a thick imperfect laminated composite ring under hydrostatic pressure. *Int. J. Solids Struct.* **40**, 7063–7092 (2003)
19. Joyce, P.J.: Experimental Investigation of Defect Critically in FRP Laminate Composites. The University of Texas at Austin, Texas (1999)
20. Cohen, D., Toombes, Y.T., Johnson, A.K., Hansen, M.F.: Pressurized ring test for composite pressure vessel hoop strength and stiffness evaluation. *J. Compos. Technol. Res.* **17**, 331–340 (1995)
21. Hull, D., Clyne, T.W.: An Introduction to Composite Materials. Cambridge University Press, (1996), ISBN 0 521 28392 2
22. Cohen, D.: Influence of filament winding parameters in composite vessel quality and strength. *Composites* **A28**, 1035–1047 (1997)
23. Zhao, L., Mantell, S.C., Cohen, D., McPeak, R.: Finite element modelling of the filament winding process. *Compos. Struct.* **52**, 499–510 (2001)
24. Li, J., Ma, H., Huang, Y.: A method for characterizes the interface between carbon fiber and epoxy resin: Three-parameters exponential pattern. *Mater. Chem. Phys.* **89**, 367–372 (2005)
25. Costa, M.L., de Almeida, S.F.M., Rezende, M.C.: The influence of porosity on the interlaminar shear strength of carbon/epoxy and carbon/bismaleimide fabric laminates. *Compos. Sci. Technol.* **61**, 2101–2108 (2001)